small structures
www.small-structures.com

Deciphering Interfacial Charge Transfer Phenomena at Nickel Nanocluster–Oxide Interface toward Augmented Efficacy in Electrochemical Water Splitting

Tapu Raihan Gazi, Mrinal Kanti Sikdar, Pijush Sardar, Ahin Roy, and Indranath Chakraborty**

The strategic engineering of heterostructure interfaces offers a promising route to surmount the activation energy barriers in water-splitting processes, thereby enhancing overall gas evolution efficiency. In this work, a nanoheterostructure comprising nickel nanoclusters (NCs) anchored on NiO nanosheets (NS) is synthesized, and electrochemical properties are evaluated. Incorporation of Ni NCs markedly augments the hydrogen and oxygen evolution reaction activities of NiO NS, primarily due to the facilitation of charge transfer across the nanocluster/oxide interface. Under alkaline conditions, optimal water-splitting performance is observed at NCs loadings upto 20 wt%, beyond which efficiency declined. Density functional theory calculations and X-ray photoelectron spectroscopy analyses reveal that the enhanced catalytic activity stems from electronic interactions between Ni NCs and NiO NS, which favor the desorption of oxygen molecules. However, excessive nanocluster deposition impedes the accessibility of the nanocluster/oxide interface. Additionally, surplus NCs increase the hydrophobicity of the heterostructure, thereby hindering essential charge transfer processes. Unlike conventional metal/oxide systems dominated by polydisperse nanoparticles, this study exploits atomically precise Ni nanoclusters, enabling well-defined interfacial sites that facilitate charge transfer and optimize *H/*OH adsorption. This atomic-level control establishes clear structure–property correlations, offering mechanistic insight into interfacial catalysis and facilitating the deliberate development of efficient water-splitting electrocatalysts.

1. Introduction

Electrochemical water splitting, a key technology for hydrogen production, represents a cornerstone in the transition toward sustainable energy sources. It involves two half-reactions: the hydrogen evolution reaction (HER) and the oxygen evolution reaction (OER).[1,2] H_2 has a high gravimetric energy density and produces negligible emissions when burned. Water splitting produces extremely pure H_2 and O_2. Renewable energy sources like solar, wind, and tidal energy can power the process for better sustainability. Developing highly efficient and cost-effective electrocatalysts for alkaline water electrolysis[3,4] is essential for sustainable hydrogen energy generation. High-performance green hydrogen generation systems face challenges because of sluggish HER/OER kinetics in alkaline electrolytes.[5–7] Therefore, we need to design effective catalysts to increase the efficiency of water electrolysis and lower related costs. Pt-based materials are currently the best electrocatalysts for HER.[8,9] Ru or Ir oxides are the best electrocatalysts for OER.[10,11] However, their high cost and limited availability hinder widespread use. Therefore, we need novel electrocatalysts for HER and OER with effective catalytic activity and durability derived from abundant, earth-abundant materials.

Atomically precise metal nanoclusters (NCs) are a novel class of nanomaterials.[12–14] Such NCs can comprise tens to hundreds of metal atoms (1–2 nm).[15–18] This field has evolved drastically, with research mostly centered on Au, Ag, and Cu based NCs.[19–21] Ni NCs protected by thiolate ligands have garnered much attention lately.[22,23] Applications

T. R. Gazi, M. K. Sikdar, I. Chakraborty
School of Nano Science and Technology
Indian Institute of Technology Kharagpur
Kharagpur 721302, India
E-mail: indranath@iitkgp.ac.in

P. Sardar, A. Roy
Material Science Centre
Indian Institute of Technology Kharagpur
Kharagpur 721302, India
E-mail: ahinroy@matsc.iitkgp.ac.in

The ORCID identification number(s) for the author(s) of this article can be found under https://doi.org/10.1002/sstr.202500489.

DOI: 10.1002/sstr.202500489

for such well-defined $Ni_n(SR)_m$ nanoclusters in photovoltaics,[24] energy conversion,[25,26] catalysis,[27–29] and sensing[30,31] seem intriguing. Here, n and m represent the number of Ni atoms and thiolate ligands, respectively. Well-defined metal nanoclusters with known crystal structures can be model catalysts to establish atomic-level structure-property correlations. It offers a deeper comprehension of the process in nanocatalysis compared to typical larger-sized nanoparticles, where atomic purity is missing. Thiolate ligand-protected NCs can self-assemble into unique geometrical structures.[32] Also, the self-assembly can improve the stability of the NCs and prevent them from dissolving or aggregating, which are crucial characteristics for long-term electrocatalytic activity.[33–35]

Due to its abundance on earth, affordability, and adjustable electrical characteristics, nickel oxide (NiO)[36] has become a viable electrocatalyst for water splitting.[37,38] Composite designs, heterostructuring, and defect engineering all increase its activity.[39,40] Compared to conventional precious-metal catalysts, heterostructures that combine transition metal NCs with metal hydroxides or oxides have become highly effective electrocatalysts for electrochemical water splitting, providing increased activity, stability, and affordability.[41,42] Nanoheterostructures of Ni NCs anchored to NiO nanosheets (Ni NC@NiO) can be an economical and effective electrocatalyst for electrochemical water splitting. These systems can improve the HER and OER processes by using the strong interfacial interactions between metallic Ni nanoclusters and NiO matrices. However, excessive NC concentration[43–45] in oxide electrocatalysts for water splitting can considerably impair performance by obstructing active sites and decreasing conductivity.

Interfacial interactions, structure, morphology, and composition affect nanocatalysis.[46] Interfacial interactions affect the electronic band structure at the interface.[47,48] The band structure influences the electron transfer process. Wang et al.[49] showcased the effect of the d-band center of various metal atoms, such as Fe, Mn, Ni, and Co, correlating the electronic structure with the electrochemical behavior of the catalyst. The strong metal–metal oxide interaction can help to adjust the binding energy of adsorbed hydrogen (*H) and hydroxyl (*OH) to the electrocatalyst.[50,51] Such metal-support interfacial interactions can induce significant electronic interaction between the support and metal, which can influence the d-band structure of the catalytically active center, and thereby facilitate the optimized adsorption and desorption of the hydrogenated and oxygenated species during a water splitting reaction.[52] A nanoheterostructure can be a powerful electrocatalyst for water splitting. A heterostructure having two-phase solid materials, one of which is 2D and the other of which is of different dimensions, will be efficient for maximizing interfacial interactions.[53,54] Electronic structure modification and geometric structure engineering can effectively increase catalyst activity.[55] Heterostructure construction of metal oxide-based catalyst has been strategically employed to improve charge generation and separation in an electrochemical process.[56] Wang et al. demonstrated that the metallic Ni^0 sites at the Ni/NiO interface significantly enhance the hydrogen evolution process.[57] Sun et al. implemented interface charge distribution modulation of Au@NiO core-shell nanoparticles that greatly improves the oxygen evolution reaction (OER) by facilitating interfacial electronic coupling and fine-tuning adsorption energetics.[58] Zhang et al. demonstrated that electronically coupled interfaces at Ag(S)@NiO/NF can effectively modulate the electronic structure of interfacial active sites, which enhances both the Volmer and Tafel steps, leading to a significant improvement in alkaline HER activity.[59] Even though significant advances have been made in developing heterostructure electrocatalysts for water splitting, a critical gap remains in the atomic-level understanding of their interfacial mechanisms. The majority of reported heterostructures consist of polydisperse nanoparticles rather than atomically precise nanoclusters. Consequently, achieving atomic-level control of interfacial active sites remains unattainable, which obscures clear structure–property correlations, limiting mechanistic insight. Atomic-level understanding of the NC–oxide interface is also lacking, preventing the systematic tuning of catalytically active sites and electron transfer pathways. Atomically precise metal NC/metal-oxide (NC/MO) interfaces are different from conventional metal/metal-oxide (M/MO) interfaces. M/MO systems typically involve polydisperse nanoparticles governed by ensemble-averaged interactions, whereas our Ni NC@NiO heterostructures leverage atomically defined clusters with discrete, superatom-like states and ligand-tuned perimeters. This precision enables direct structure–property correlations and reveals how cluster–oxide contacts modulate charge transfer, *H/*OH adsorption, and catalytic kinetics phenomena largely inaccessible in nanoparticle systems. Addressing these research gaps through detailed mechanistic understanding at the atomic scale will enable the systematic design of catalysts with enhanced performance, accelerating the development of efficient and cost-effective water-splitting technologies.

This study involves the design and fabrication of atomically precise Ni NC@NiO heterostructures to enhance interfacial electron transfer, optimize *H/*OH adsorption, and elevate electrocatalytic performance. By integrating precise atomic structures with engineered metal–oxide interfaces, the Ni NC@NiO nanoheterostructures exhibit strong HER and OER activity under alkaline conditions. Using a combination of first-principles calculations and electrochemical experiments, comprehensive mechanistic insights into the activity have been provided.

2. Results and Discussion

2.1. Material Characterizations

An atomically precise $Ni_6(SC_{12}H_{25})_{12}$ NC was synthesized via a previously reported method[60] with 1-dodecanethiol (DDT) as a protecting ligand. The as-prepared NCs were extracted in dichloromethane (DCM) solvent, and the brown-colored NCs exhibited molecule-like optical absorption features in their absorption spectrum (Figure S1, Supporting Information) with sharp absorption peaks at 337 and 408 nm, and a broad absorption band at 552 nm. The NC was crystallized by dissolving it in DCM and kept at 4 °C. After 48 h, millimeter-sized, brown-colored, needle-shaped crystals (Figure S2, Supporting Information) were obtained for further structural analysis. Single-crystal X-ray diffraction (SCXRD) measurements revealed that the NC was crystallized in a triclinic unit cell (Figure S3, Supporting Information) with the space group of $P\bar{1}$. Detailed

crystallographic data[61] are summarized in the supporting document (Table S1–S5, Supporting Information). The NC's molecular structure (**Figure 1**a) consists of a cyclic Ni_6 core surrounded by thiolate shells. Six Ni atoms are connected in a 2D hexagonal array, and each Ni atom is linked to four bridging S atoms. Twelve thiolate ligands are present in six $SC_{12}H_{25}$-Ni-$SC_{12}H_{25}$ staples. Pairs of sulfur atoms are evenly distributed above and below the plane of the Ni_6 hexagonal ring, forming a crown-like structure (Figure 1b). The average Ni—Ni bond length (Figure S4, Supporting Information) is 2.94 Å, and that of the Ni—S bond is 2.197 Å. Large area crystal packing (Figure 1c) showed ABC... ABC type packing of NCs through CH...CH nonbonded van der Waals (vdW) interactions, as shown in Figure 1d. These intermolecular noncovalent interactions between ligands help direct the spatial arrangement of NCs, leading to the formation of densely packed, ordered (Figure S5, Supporting Information) self-assembled structures of NCs, often referred to as cluster-assembled materials (CAMs).[62–67] The morphology of this NC-based CAM was analyzed using the field emission scanning electron microscopy (FESEM) and high-resolution transmission electron microscopy (HRTEM) images. Figure S6 and S7, Supporting Information, showed 2D plate-like CAMs. Furthermore, SEM energy-dispersive X-ray spectroscopy (EDS) elemental mapping (Figure S8, Supporting Information) revealed the presence of Ni, C, and S elements, which confirms that these 2D plates are constructed by the ordered assembly of distinct $Ni_6(SC_{12}H_{25})_{12}$ NCs (Ni NCs). Nickel oxide (NiO) nanosheets (NS) were synthesized using the reported method[68,69] and primarily characterized by powder X-ray diffraction (PXRD). The diffractogram (**Figure 2**m) contains peaks at 37.1°, 43.2°, and 62.4°, corresponding to the (111), (200), and (220) crystal planes of the NiO (JCPDS 47-1049). The FESEM images of the NiO (Figure S9, Supporting Information) showed uniform nanoflake oxide particles.

To understand the dynamics of Ni NCs at the oxide interface, these NCs were grafted on NiO NS with a varied concentration of Ni NCs, which were characterized (Figure S10–S16, Supporting Information). This NC-NS heterostructure with different NC concentrations was then deposited on Ni-foam to check its electrochemical performance. Figure 2 summarizes the electron microscopy and elemental analysis of the Ni NC@NiO heterostructure deposited on the Ni foam. The EDS mapping shows the distribution of S and C, which comes from the NC's organic part, and suggests the presence of NC on the electrode surface without segregation during the electrode formation. To enhance understanding of the elemental distribution and to verify the integration of Ni NCs into the heterostructure, ToF-SIMS mapping (Figure 2i–k, S13, S14, Supporting Information) was conducted. The spectra and spatial maps distinctly indicate the existence of Ni and S signals, confirming the effective incorporation of Ni NCs onto the NiO nanosheets and substantiating the uniform development of the heterostructure. To investigate the role of ligands and the thermal stability of the heterostructure, thermogravimetric analysis (TGA) was performed on Ni NCs and NiO nanosheets, as well as on the Ni NC@NiO heterostructure (Figure S16, Supporting Information). The TGA of Ni NCs exhibits multistep mass losses of ≈85–88% between 200 and 650 °C, with a final plateau residue of ≈12–13%, which is in excellent agreement with the theoretical Ni_6 content of the nanocluster core (12.7 wt%), confirming the stable nature of the Ni NCs. The significant weight loss noted between 200 and 300 °C is attributed to the decomposition of dodecanethiol

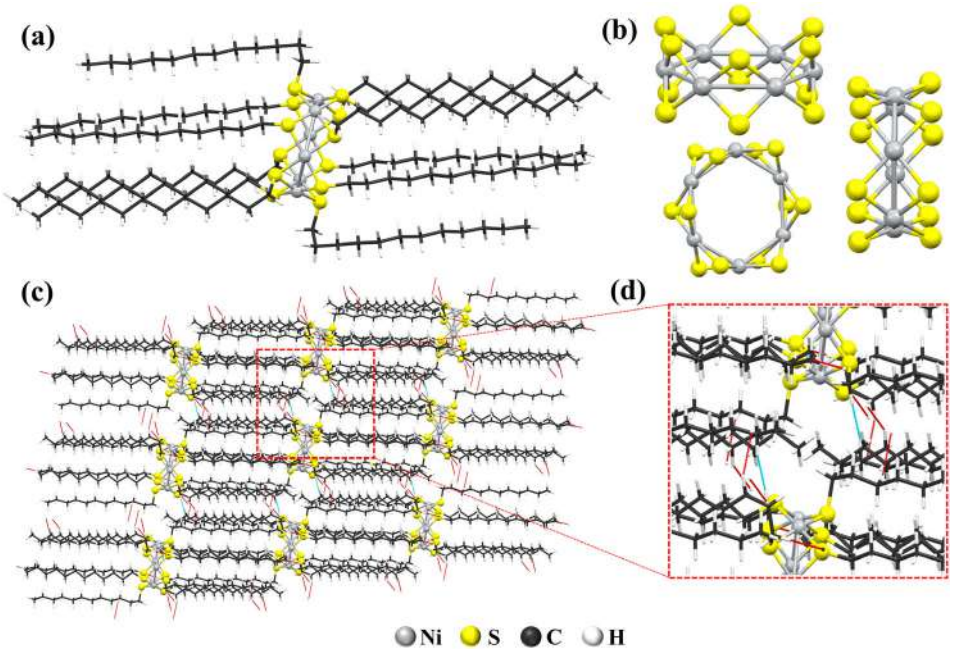

Figure 1. a) Total structure of $Ni_6(SC_{12}H_{25})_{12}$ nanocluster crystalized in DCM. b) Different views of the rings with the ligand functionalities. c) Structural view of a self-assembled large area crystal packing of the Ni NCs, and d) a zoomed view shows different types of vdW interactions between the nanoclusters.

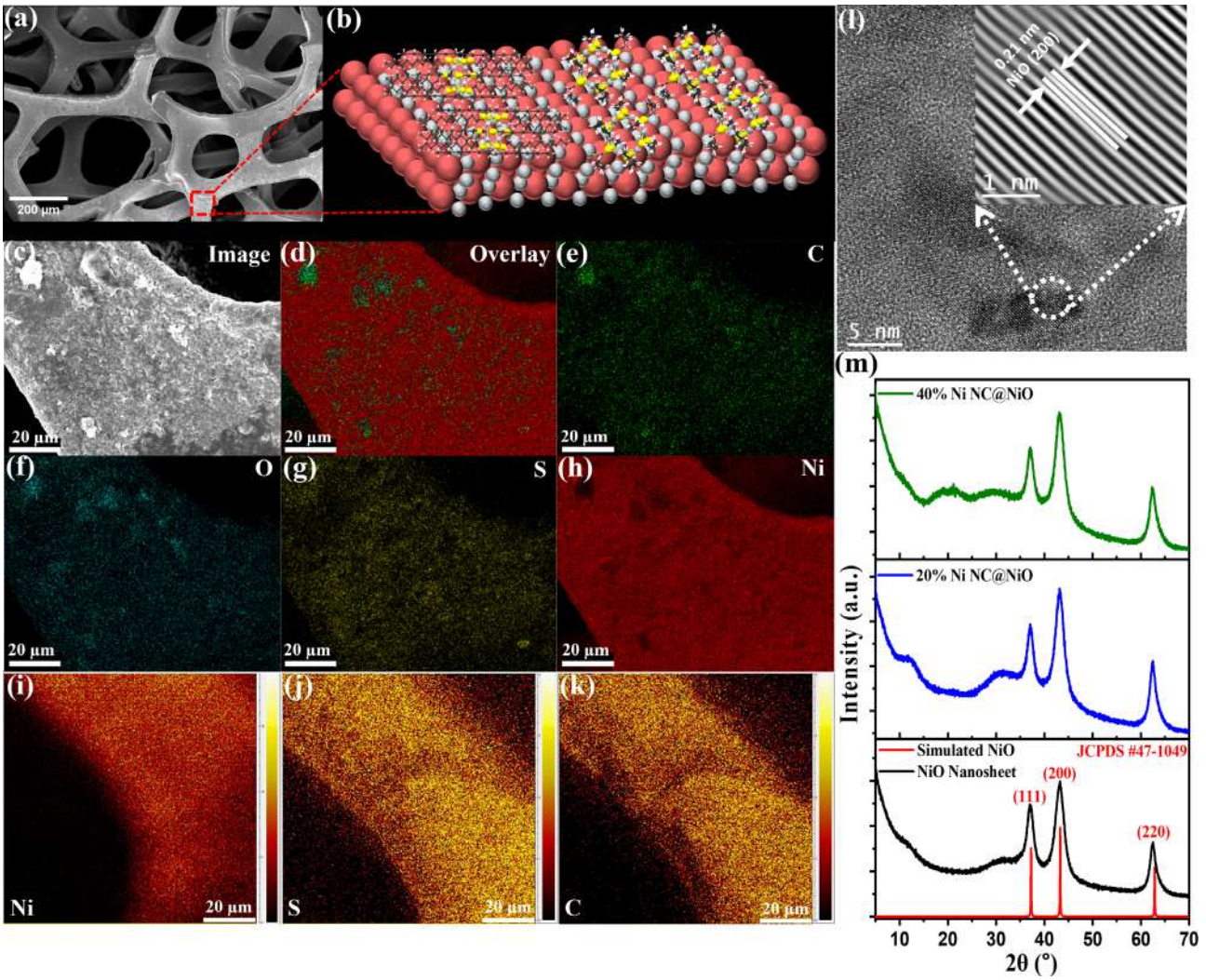

Figure 2. a) FESEM micrograph of the Ni NC@NiO nanoheterostructure deposited on Ni foam. b) Schematic illustration of the nanoheterostructure deposited on Ni foam. c) FESEM micrograph of an area selected for EDS mapping of the nanoheterostructure deposited on Ni foam. d) An overlay of the selected area EDS mapping and the corresponding elemental mapping of e) C (green), f) O (blue), g) S (yellow), and h) Ni (red). ToF-SIMS elemental mapping of the 20% Ni NC@NiO heterostructure catalyst dropcasted on a Ni foam. The maps show the spatial distribution of i) Ni, j) S, and k) C elements across the selected electrode surface. l) HRTEM image of 20% Ni NC@ NiO heterostructure particle surface and calculated lattice fringe. m) Powder XRD patterns of NiO nanosheet, 20% Ni NC@NiO, and 40% Ni NC@NiO.

(DDT) ligands. NiO nanosheets exhibit significant thermal stability, maintaining integrity up to 900 °C, with ≈12% weight loss attributed to the desorption of moisture and hydroxyl groups. The TGA profile of the Ni NC@NiO heterostructures exhibits intermediate behavior relative to the two individual components. The 20% Ni NC@NiO composite demonstrates a final residue of ≈73–74% at 900 °C, aligning closely with the theoretical value of 73.6% derived from the neat-component TGAs (NiO residue and the Ni_6 fraction in $Ni_6(SC_{12}H_{25})_{12}$). All of the heterostructures exhibit a distinct multistep mass loss in the 200–500 °C range, directly correlating with the coexistence of thiolate ligands. 2D plate-like CAMs were seen under HRTEM (Figure S7, Supporting Information). The FFT pattern displays several polycrystalline rings, which reflect the presence of numerous small crystallites oriented randomly. Figure 2l and S11, Supporting Information, present the HRTEM images of the 20% Ni NC@NiO sample, and analysis of its lattice fringes reveals a spacing of 0.21 nm, attributed to the (200) plane of NiO. X-ray photoelectron spectroscopy (XPS) analysis was carried out to investigate the detailed elemental and structural information of NiO and the resulting heterostructure material. The Ni 2p spectrum (**Figure 3**a) consists of two spin multiplets (via spin-orbit coupling): $2p_{3/2}$ and $2p_{1/2}$, spanning from 852 to 865 eV and 870 to 880 eV, respectively. For NiO, peaks at 853.49 eV, 870.95 eV, and their corresponding satellite peaks are responsible for the Ni^{2+} of the NiO lattice. However, peaks at 855.17 and 872.7 eV and their satellite peaks are assigned to the Ni^{3+} state, indicating the presence of another NiOOH phase. For Ni NC@NiO heterostructure material, the peaks corresponding to Ni^{2+} and Ni^{3+} come at higher binding energy values at

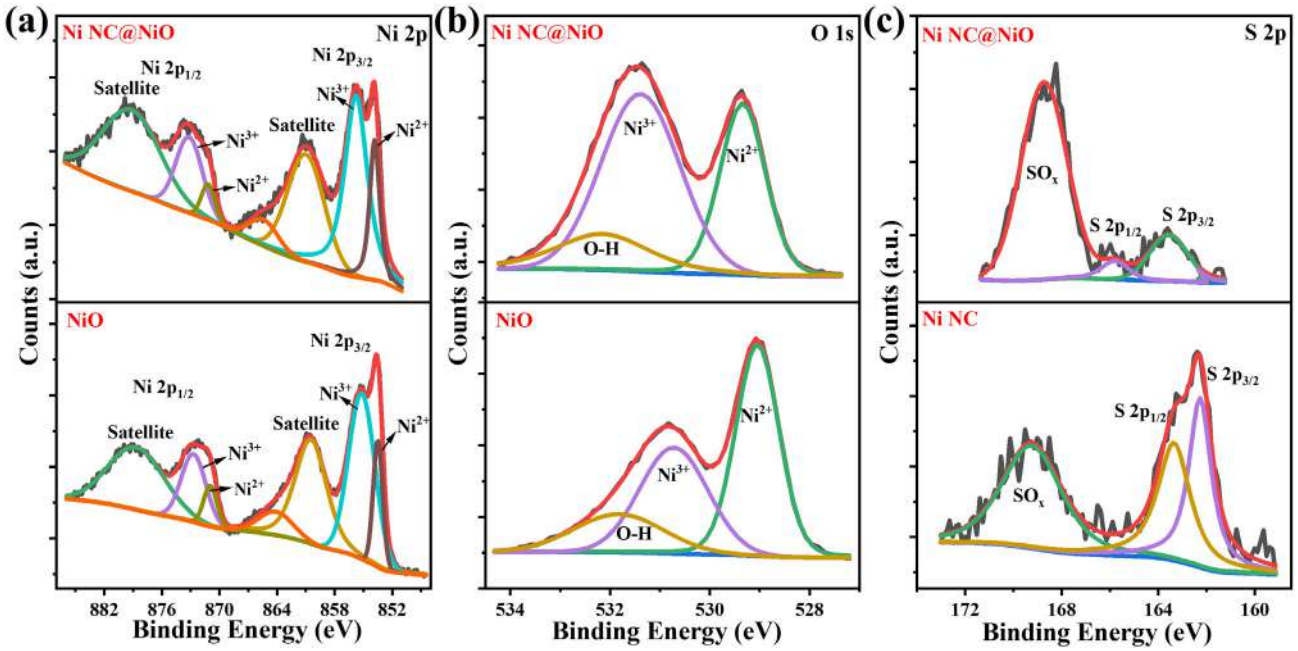

Figure 3. Deconvoluted XPS spectra of a) Ni 2p, b) O 1s, and c) S 2p for Ni NC, NiO, and Ni NC@ NiO heterostructure.

853.82, 871.17, 855.77, and 873.16 eV, respectively. This positive chemical shift of Ni 2p in the heterostructure material suggested a downshift of the d-band center of Ni,[52] resulting from the interaction of thiol groups of the NCs with the surface Ni atoms of NiO.[23,70] Figure 3b exhibits the deconvoluted XPS spectrum of O 1s, which contains three distinct peaks for different states of O. The peak at 529.04 eV is ascribed to the Ni—O—Ni of the NiO crystal structure. The other peak at 530.72 eV can be assigned to the O atoms with the Ni atoms in +3 oxidation states, which can be created due to a nickel vacancy in the NiO surface.[71,72] Another small peak at 531.82 eV corresponds to the O—H of the adsorbed oxygen species or adsorbed water.[73] Similar to the Ni 2p spectra, positive chemical shifts for the O 1s spectra in the Ni NC@NiO heterostructure depict significant charge transfer from NiO to Ni NCs through an interfacial heterojunction.[23,74] In this case, the peak intensity for the Ni^{3+}-O peak has been enhanced compared to the pristine NiO, which confirms that the inclusion of NCs causes Ni vacancies and induces surface defects in NiO that can subsequently improve the charge transfer kinetics at the interface.[23,71,72,75] For Ni NCs, S 2p high-resolution XPS peak fitting (Figure 3c) also reveals multiple peaks at 162.27 and 163.35 eV corresponding to the S $2p_{3/2}$ and S $2p_{1/2}$ of Ni-S unit, along with an additional peak at 169.239 eV, which is responsible for the oxidized sulfur species[76–78] originating from air and moisture exposure.

2.2. Evaluation of the Electrocatalytic Performance

The electrocatalytic performance of NiO nanosheets and the Ni NC@NiO nanoheterostructure was evaluated in 1 M KOH electrolyte in a conventional three-electrode system at a scan rate of 50 mV s^{-1}. For electrocatalytic HER (**Figure 4**a, S23a, S24a, Supporting Information), the pristine NiO nanosheet exhibited an overpotential of 550 mV for a 100 mA cm^{-2} current density. Meanwhile, the Ni NC@NiO nanoheterostructure improved performance compared to the pristine NiO. The Ni NC@NiO displays a significantly lower overpotential of 396 mV at 100 mA cm^{-2} current density. This higher HER activity is primarily because of the faster charge transfer across the NiO and Ni NC heterointerface. The composition of the heterostructure was also varied by increasing the concentration of the NCs. The electrocatalytic activity was checked for 10–40% of the Ni NCs loading. The HER activity increased for the heterostructure up to 20% of the Ni NC loading, and the performance decreased gradually for higher NC loading up to 40%. The 20% Ni NC@NiO delivered the best HER performance among all the heterostructures, exhibiting an overpotential of 396 mV at 100 mA cm^{-2} current density. The HER overpotential of all the electrodes follows the order: 20% Ni NC@NiO (396 mV) < 10% Ni NC@NiO (484 mV) < NiO (502 mV) < 30% Ni NC@NiO (508 mV) < 40% Ni NC@NiO (533 mV) < Bare Ni foam (596 mV). Thus, the 20% Ni NC loading is the optimized concentration for the superior HER activity, and the overpotential is 106 mV lower than that of NiO. After normalizing the LSV curves by the electrochemical surface area (ECSA) to eliminate the influence of surface area, Figure 4c reveals that 20% Ni NC@NiO delivers better HER activity compared to other electrodes. This suggests that the superior performance arises not only from a larger ECSA but also from the enhanced intrinsic catalytic activity, which can be ascribed to the optimized electronic structure.[52] The 40% Ni NC-loaded heterostructure, on the other hand, has the lowest electrocatalytic activity and the highest overpotential (533 mV). This activity degradation for 40% Ni NC@NiO can be addressed by decreased electrical conductivity and increased hydrophobicity in the electrode-electrolyte interface upon excessive NCs loading, as the NCs are protected by dodecanethiol ligand.

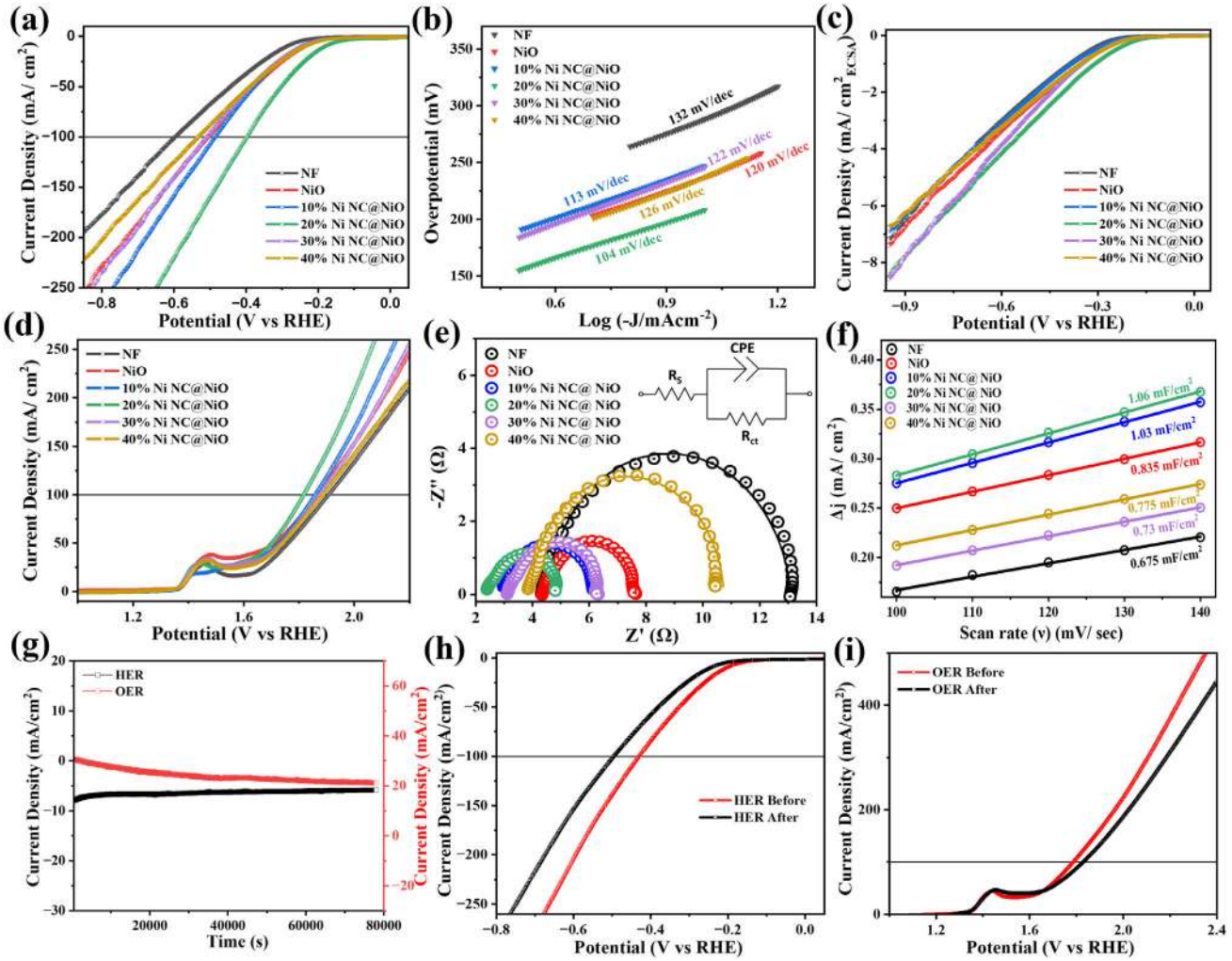

Figure 4. Electrocatalytic performance of the Ni NC@NiO nanoheterostructure deposited on NF. a) LSV curves of different nanoheterostructures with varying Ni NCs loading for HER in 1 M KOH. b) Corresponding HER Tafel plots of the nanoheterostructures. c) ECSA-normalized LSV plots for HER. d) LSV curves of different nanoheterostructures with varying Ni NC loading for OER in 1 M KOH. e) Nyquist plots for the nanoheterostructures in 1 M KOH. (The dots show the experimental points; the solid line shows the fitted curve.) f) Capacitive currents versus scan rates plot and the C_{dl} estimation for the nanoheterostructures. g) Chronoamperometry plots of the 20% Ni NC@NiO electrode for HER and OER, and the LSV polarization plot before and after the chronoamperometric stability test for h) HER and i) OER.

To study the reaction kinetics of the HER, the Tafel slope was determined using the HER polarization curve (Figure 4b). The Tafel slope gives information about the charge transfer kinetics and rate-limiting step of the HER reaction on the electrode surface.[79,80] From the Tafel slope analysis, it is evident that the 20% Ni NC@NiO showed a Tafel slope of 104 mV dec^{-1}, which is relatively less than the pristine NiO nanosheets (120 mV dec^{-1}). The lower Tafel slope of the 20% Ni NC@NiO electrode suggests that the charge transfer reaction kinetics become faster with the addition of the $Ni_6(SC_{12}H_{25})_{12}$ NCs. The Tafel slope value (104 mV dec^{-1}) of the 20% Ni NC@NiO electrode indicates that the HER is controlled by a coupled Volmer–Heyrovsky type mechanism,[81] with the Volmer step being predominantly the rate-determining step (RDS) for the electrochemical HER reaction in the alkaline medium. The electrocatalytic OER efficiency of the Ni NC-based heterostructure (Figure 4d and S25, Supporting Information) was also investigated in a 1 M KOH solution. The pristine NiO nanosheets showed an overpotential of 638 mV at 100 mA cm^{-2} current density. In this case, the 20% Ni NC@NiO heterostructure displayed significantly better OER activity than other NiO and heterostructures. The overpotential of the 20% Ni NC@NiO nanoheterostructure was 586 mV for a 100 mA cm^{-2} current density. A similar trend of electrocatalytic activity was observed for OER. With 40% of the NCs loading, an overpotential of 656 mV was obtained, 70 mV higher than the best-performing heterostructure. The optimized 20% Ni NC@NiO heterostructure has competitive overpotentials at 100 mA cm^{-2} when compared (Figure S26, Supporting Information) to benchmark catalysts Pt/C (HER) and RuO_2 and IrO_2 (OER), highlighting its potential as a cost-effective substitute for noble-metal catalysts.[82–84]

The electrochemical behavior of the Ni NC-based heterostructure was further investigated by electrochemically active surface area (ECSA). The ECSA is related to the electrodes' double-layer capacitance (C_{dl}).[74,85] The C_{dl} was determined by measuring cyclic voltammograms (CV) at different scan rates (100–140 mV s^{-1}) in a non-faradaic region. C_{dl} values were obtained using the CV plots' slopes (Figure S22, Supporting Information) and the cathodic and anodic current densities.[85,86] The ΔJ versus scan rate plot (Figure 4f) revealed that the 20% Ni NC@NiO electrode has a C_{dl} value of 1.06 mF cm^{-2}, the highest of all the electrodes. So, the C_{dl} value suggested that the 20% Ni NC@NiO heterostructure possesses more active sites and active surface area for facilitating the electrochemical reactions in the electrode-electrolyte interface. The obtained C_{dl} values for other electrodes are 1.03, 0.835, 0.775, 0.73, and 0.675 mF cm^{-2} for 10% Ni NC@NiO, NiO, 40% Ni NC@NiO, 30% Ni NC@NiO, and Bare Ni foam, respectively. These values align with the observed electrocatalytic HER and OER activity trend. Electrochemical impedance spectroscopy (EIS) was also performed to study the charge-transfer kinetics at the electrode. The Nyquist plot (Figure 4e, S23b, S24b, Supporting Information) shows that the 20% Ni NC@NiO heterostructure electrode displays the smallest semicircle among all the electrodes, offering a lower charge transfer resistance (R_{ct}) value of 2.51 Ω. As a result, the charge transfer kinetics at the 20% Ni NC@NiO electrode interface are much faster, mainly due to the facile electronic interaction between the NiO and the Ni NC. Upon increasing NCs loading, the R_{ct} value gradually decreases up to 20% of the NCs loading. But there is a rise in R_{ct} value for higher NCs loading, which can be addressed as the reduced interfacial interaction of the $Ni_6(SC_{12}H_{25})_{12}$ NCs with the NiO nanosheets because of the long-chain bulky hydrocarbon ligand of the NC. So, the activity loss for HER and OER results from poor electrical conductivity upon excessive NCs loading.

The stability of the electrode is another crucial element that evaluates an electrocatalyst's performance. Thus, chronoamperometry measurements (Figure 4g) were carried out for the 20% Ni NC@NiO heterostructure at a fixed potential to investigate the long-term stability of the electrode. The heterostructure electrode delivered a very steady performance for 78000 s and maintained ≈75% of the initial current density for both HER and the OER, confirming the durability of the heterostructure under prolonged electrocatalysis experiments. Furthermore, poststability characterizations were investigated to assess the structural integrity of the catalyst. SEM imaging, along with EDS elemental mapping (Figure S17–S19, Supporting Information) of the electrode, indicates that both Ni nanoclusters and NiO nanosheets remain intact and uniformly distributed on the Ni foam support. The electrodes preserve the nanosheet morphology of the heterostructures, confirming their morphological stability under extended electrochemical conditions. EDS mapping again confirms the presence of well-distributed Ni, O, S, and C elements, corresponding to the NiO and Ni NCs. ToF-SIMS analysis (Figure S20–S21, Supporting Information) further confirms the presence of Ni, S, C, and O signals in positive and negative modes, indicating the structural integrity of the heterostructure during electrocatalysis. Further, we have also performed poststability electrochemical experiments such as LSV and EIS plots (Figure 4h,i and S27, Supporting Information) after 78000 s of chronoamperometry, revealing a modest rise in charge-transfer resistance and a minor shift in overpotential relative to the initial electrode. These findings indicate that the catalyst retains most of its electrochemical activity even after extended operation, further validating the robustness of the heterostructure electrocatalyst. Additionally, a CV cycling stability test (Figure S28, Supporting Information) was carried out over 3500 consecutive cycles to assess the long-term durability of the catalyst. The post-CV polarization curves (Figure S29, Supporting Information) also validate the durability and stable catalytic activity for the Ni NC@NiO heterostructure electrode.

2.3. DFT Simulations for the Catalysis Mechanism

The nickel NC ($Ni_6(SC_{12}H_{25})_{12}$)[60] considered in this experiment contains a closed nickel-sulfur cage containing six Ni and twelve S atoms, functionalized with 12 dodecyl groups linked with the 12 S atoms. To model the NC through first-principles simulation, we considered 6 Ni atoms caged with 12 S atoms followed by the actual nanocluster. But instead of functionalizing the S atoms with dodecyl group, we rather used methyl groups to terminate six non-adsorbing S atoms, forming $Ni_6S_{12}(CH_3)_6$ structure, and the structure was optimized in density functional theory (DFT) simulation (**Figure 5**b). To look into the steric effects, we have also calculated the C_2H_5 group passivated single unit Ni NC in contrast to the CH_3 group, and the d-band profiles do not vary significantly, as shown in Figure S31, Supporting Information. Hence, to probe electronic interactions, we proceed further with the CH_3 passivation. Also, according to literature,[87] the NiO-100 surface is the most stable (Figure S30, Supporting Information), with the least surface energy. Hence for further simulations, we have used the NiO-(100) as our model surface. Adsorption of the NC onto the NiO (100) surface leads to strong binding and surface reconstitution for the NiO. The charge density difference plot illustrated in Figure 5e validates strong electronic interaction of the Ni nanocluster with bare NiO surface. The charge density difference calculation at the NiO surface due to nanocluster adsorption was done utilizing the formula

$$\rho_{dif} = \rho_{total} - \rho_{surface} - \rho_{molecule} \quad (1)$$

where ρ_{total} represents the total charge density of the nanocluster adsorbed NiO system and $\rho_{surface}$ and $\rho_{molecule}$ correspondingly represent the charge density of bare NiO and isolated nanocluster unit. The HER and OER activities were modeled with these two systems to understand the differences in the activity of NiO and NCs-adsorbed NiO toward water splitting in alkaline medium. Figure 5a,b shows the relaxed structures of NiO-(001) surface and the modeled Ni-based cluster, respectively. The NC-adsorbed structure of the NiO surface is shown in Figure 5c.

The calculation of free energy changes of HER intermediates in alkaline medium involved the following steps[88]

Step-1: $*H_2O \rightarrow *OH + *H$

Step-2: $*OH + *H \rightarrow OH^- + *H$

Step-3: $OH^- + *H \rightarrow OH^- + 1/2\ H_2$

Figure 5d shows the energy landscape of the reaction for bare NiO surface and NCs-adsorbed NiO surface; the corresponding

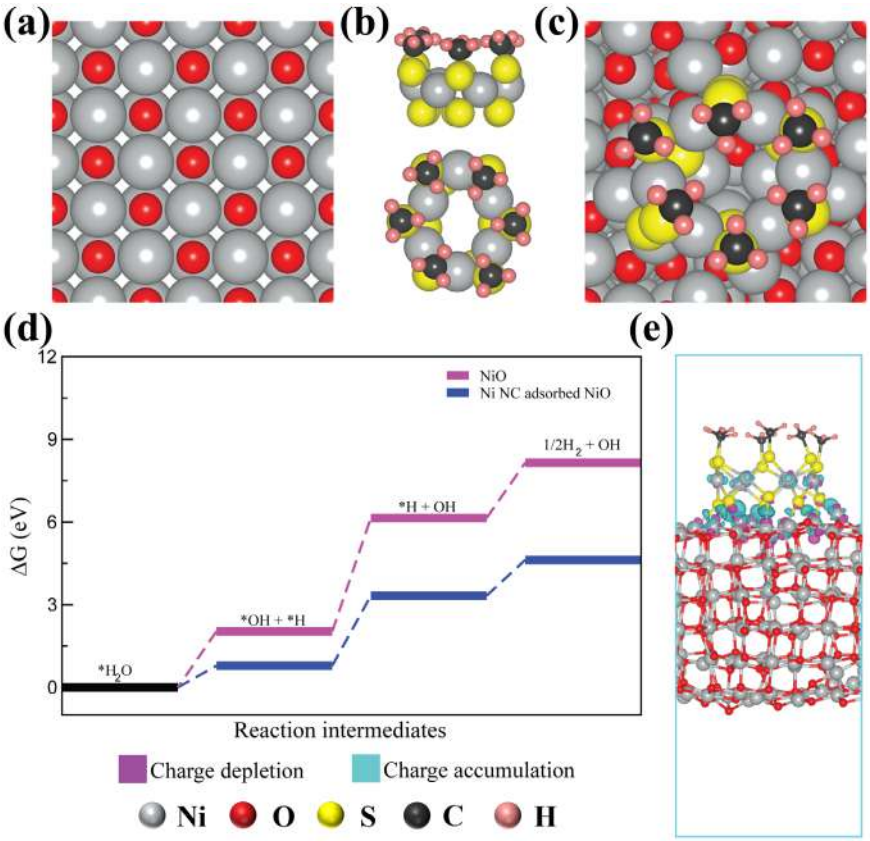

Figure 5. a–c) The bare NiO surface (100), modeled unit of Ni NCs, and NiO (100) surface after NCs adsorption. Plot (d) illustrates the free energy difference diagram of HER intermediates for both the bare and NC-adsorbed NiO surface in alkaline medium; e) charge accumulation-depletion on the NiO surface showing strong interaction of NC with the surface—the isosurface level for the plot is 0.01 e^{-} $Å^{-3}$.

optimized structures are shown in Figure S33, Supporting Information. For HER in the alkaline medium, H_2O adsorption has been carried out on different systems, viz. NC adsorbed NiO surface, bare NiO surface, and free NC have been calculated. Our calculations reveal that H_2O adsorption is not feasible on free NC. Figure S34, Supporting Information, shows the H_2O-bound structures of NiO and Ni NC@NiO. We have computed further steps with the two systems. Compared to bare NiO, Ni NCs-adsorbed NiO shows a lower free energy barrier for all the intermediate steps of HER in alkaline medium. Remarkably, the barrier decreases significantly for the NCs adsorbed surface (by 3.53 eV) for the last step. This indicates NC adsorption-mediated enhancement of the HER performance of bare NiO by facilitating the H_2 desorption. The other part of the water splitting, that is, oxygen evolution reaction (OER), was modeled through a 4 e^{-} pathway[89] as the experiments were carried out in alkaline medium

$$4OH^{-} \rightarrow O_2 + 2H_2O + 4e^{-}$$

The four intermediate steps considered for this reaction are the following

Step-1: $* + OH^{-} \rightarrow *OH + e^{-}$
Step-2: $*OH + OH^{-} \rightarrow *O + H_2O + e^{-}$
Step-3: $*O + OH^{-} \rightarrow *OOH + e^{-}$
Step-4: $*OOH + OH^{-} \rightarrow * + O_2 + H_2O + e^{-}$

The change in free energy for all these four intermediate steps (**Figure 6**h) was calculated, and it was evident that Ni NCs adsorbed NiO show an energetically downhill process for OER, whereas for the bare NiO surface, the formation of the *OOH intermediate and subsequently O_2 formation are energetically uphill process. This renders the NC-adsorbed surface a better catalyst for both HER and OER.

To understand the electronic origin of the better OER activity upon cluster adsorption, l-decomposed atom projected density of state analysis was done over the d-orbitals of the surface Ni atom for the case of both bare NiO and NCs adsorbed NiO along with the d-band center, utilizing the formula[90]

$$E_{\mathrm{d-BC}} = \frac{\int_{E_1}^{E_2} g(E) E dE}{\int_{E_1}^{E_2} g(E) dE} \tag{2}$$

where $g(E)$ represents the density of states of the d-band electrons within the energy interval E_1 to E_2 with respect to the Fermi level. Upon calculating the d-band center, we found a −0.35 eV shift in the d-band center (Figure 6g) when we consider NCs adsorption on top of bare NiO. This suggests reduced reactivity of surface Ni atoms of NiO due to cluster adsorption, hence better OER performance.

Also, the shift in the d-band center was calculated for all four reaction intermediates in the case of both the bare and Ni

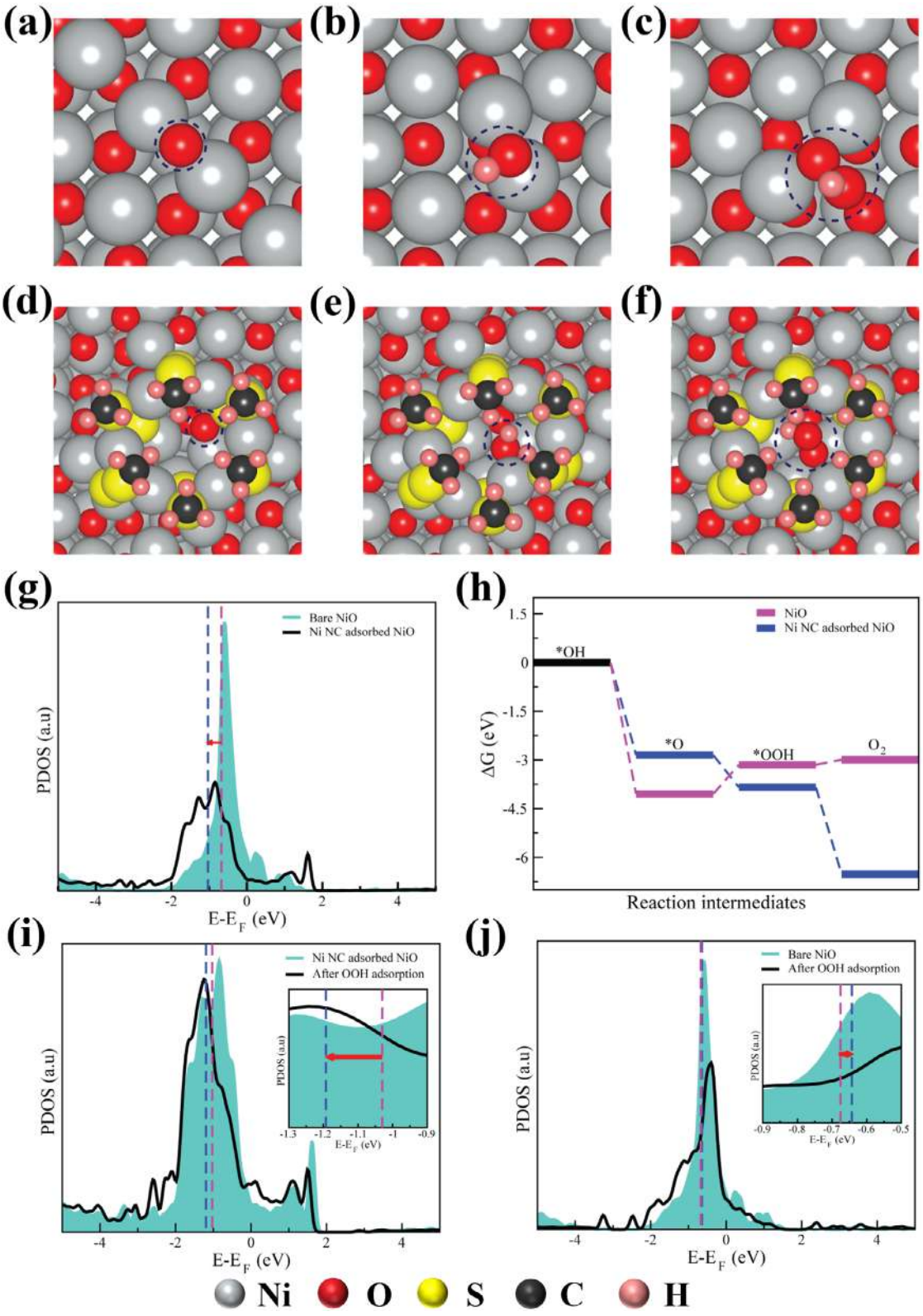

Figure 6. a–c) The OER intermediates (*O, *OH, and *OOH) adsorbed over the bare NiO surface. d–f) The same, but over the Ni NCs adsorbed NiO surface. g) Projected density of states plot of the surface Ni atom for both bare NiO and NCs adsorbed NiO. h) The free energy difference plot of OER intermediates for both surfaces accordingly. i,j) The shift in the d-band center of the surface Ni atom of NiO due to *OOH adsorption over both NCs adsorbed NiO and bare NiO.

Table 1. Shift in d-band center due to the adsorption of OER intermediates for both the bare and Ni NCs adsorbed NiO surface.

Bare NiO surface		Ni NCs adsorbed on the NiO surface	
Adsorbed intermediates	Shift in d-band center [eV]	Adsorbed intermediates	Shift in d-band center [eV]
*OH	–0.157	*OH	–0.276
*O	–0.397	*O	–0.145
*OOH	0.033	*OOH	–0.163

NCs-adsorbed NiO surfaces. The corresponding values are reported in **Table 1**. From Figure 6i,j, we found that for bare NiO, *OOH adsorption leads to a positive shift of the d-band center of the surface Ni atom, while the same goes toward a negative direction due to Ni NCs adsorption. This inversion of the d-band center shift significantly highlights the enhanced OER activity of NiO due to NCs adsorption. For the other two OER intermediates, we found a more negative d-band shift during O adsorption for the bare NiO surface. In contrast, during OH adsorption, this trend goes opposite (Figure S35, Supporting Information). The charge density difference plots for OER intermediates in bare and Ni nanocluster-activated NiO surfaces are given in Figure S36, Supporting Information, to understand the reaction pathway better. In summary, for both the HER and OER, owing to the electronic interaction of the adsorbed cluster and the NiO surface, the catalytic activity improves, rendering the adsorbed system a better catalyst.

However, when NCs are densely packed, they can hinder the diffusion of reactants to active sites.[91,92] Excessive Ni NC loading onto the NiO nanosheet matrix can block the active Ni NC@NiO interface. Ligands play a crucial role in stabilizing NCs and tuning their electronic properties. However, excess ligands can also block active sites or interfere with reactant adsorption, hindering electrocatalytic performance. So, excessive NCs can hinder electron transport due to increased resistance or blockage of pathways, leading to slower reaction kinetics and reduced performance. Thiolated NCs can be hydrophobic, particularly when the thiol groups are attached to long alkyl chains.[93] These long chains increase the overall hydrophobicity of the cluster, making it insoluble in water and more soluble in nonpolar solvents. However, thiol groups themselves are not inherently hydrophobic; they are slightly polar and can form weak hydrogen bonds, but the attached alkyl chains' hydrophobic nature dominates the cluster's overall behavior. So, excessive clusters can also increase the overall hydrophobicity of the heterostructure and decrease the catalytic performance. In the presence of excess NCs, the sulfur can also block the nickel in NiO. The strong sulfur-metal bond can lead to a substantial or complete loss of catalytic activity. Hence, optimizing the concentration of NCs is critical to maximizing the catalytic activity of such nanoheterostructure materials.

3. Conclusion

A base-stable $Ni_6(SC_{12}H_{25})_{12}$ NC was synthesized, and its crystal structure was resolved via single-crystal X-ray diffraction. The NCs self-assemble through intermolecular noncovalent ligand interactions. Incorporating these Ni NCs onto NiO nanosheets enabled us to evaluate their electrocatalytic activity, revealing that a 20 wt% NCs loading on NiO achieves optimal HER and OER performance in 1 M KOH. DFT calculations indicate strong binding between the NCs and the NiO surface, with a notable shift in the d-band center of surface Ni atoms upon cluster adsorption enhances electrocatalytic activity. However, higher loadings can increase hydrophobicity at the interface, impeding HER and OER processes. This work offers detailed insights into the mechanisms governing HER and OER in oxide/thiol-protected non-noble metal NC heterostructures. Importantly, these findings advance our understanding of charge transfer dynamics at the nickel NC–oxide interface, revealing how interfacial electronic interactions and their modulation govern catalytic activity. Optimizing key parameters of atomically precise metal nanocluster-based catalysts, such as their structural features, the orientation of organic ligands, nanocluster concentration, and catalyst selectivity, could open new pathways for developing next-generation electrocatalysts. The deliberate design of nanocluster architectures combined with tailored interfacial ligand chemistry aims to fully unlock the catalytic potential of Ni nanocluster-based heterostructures, facilitating the creation of cost-effective and advanced electrocatalysts.

4. Experimental Section

Chemicals and Materials: Nickel(II) acetylacetonate [Ni(acac); ($Ni(C_5H_7O_2)_2$)], oleylamine (OAm), and 1-dodecanethiol (DDT, 98%) were obtained from Sigma–Aldrich. $Ni(NO_3)_2{\cdot}6H_2O$, urea, ethylene glycol, dichloromethane (DCM), and ethanol were obtained from SRL chemicals. Ultrapure Milli-Q water (18.2 MΩcm) was used throughout the entire experiment.

Synthesis of $Ni_6(SC_{12}H_{25})_{12}$ Nanoclusters: This study implemented the wet-chemical synthesis approach to synthesize the atomically precise Ni NC protected by a 1-dodecanethiol ligand.[60] For the NC synthesis, 0.1 mmol of $Ni(acac)_2$ was dissolved in 10.0 mL OAm under ultrasonication. The reaction mixture was heated at 120 °C for 15 min with vigorous stirring, and the color of the solution turned light green from light blue. Then 1-dodecanethiol (250 µL, 1 mmol) was added dropwise into the round-bottom flask under constant stirring. The color of the solution changes from light green to brown after 5 min. Subsequently, the solution was stirred at 120 °C for 6 h, cooled to room temperature, and a substantial quantity of ethanol was introduced to the dark-brown reaction mixture to produce a red-brown precipitate. The $Ni_6(SC_{12}H_{25})_{12}$ NCs were collected through centrifugation at 10000 rpm and washed with ethanol. Finally, a dark brown NC solution was obtained by extracting the product with dichloromethane.

Synthesis of NiO Nanosheets: $Ni(NO_3)_2{\cdot}6\,H_2O$ (400 mg) and urea (165.2 mg) were dissolved in 30 mL of EG. Continuous stirring added 20 mL of Milli-Q water to the above solution. The reaction mixture was transferred into a 100 mL Teflon-lined stainless-steel autoclave and heated at 140 °C for 7 h. After cooling to room temperature, the green-colored product was centrifuged, washed with water and ethanol several times, and dried at 60 °C overnight. The powder was calcined in air at 300 °C for 3 h to produce the NiO nanosheets.[68,69]

Synthesis of Ni NC@NiO Heterostructure: For the preparation of the Ni NC@NiO heterostructure, 8 mg of NiO nanosheets were dispersed in 2 mL of $Ni_6(SC_{12}H_{25})_{12}$ nanocluster solution (1 mg mL^{-1}) with continuous stirring. The mixture was treated under ultrasonic treatment for 30 min to enhance the uniform interaction and anchoring of Ni nanoclusters on the NiO nanosheet surface. The product was isolated through centrifugation, subsequently washed with DCM, ethanol, and deionized water to eliminate

excess ligands, and finally dried under vacuum conditions. The successful integration of Ni NCs into NiO was characterized through TGA, SEM–EDS elemental mapping, and ToF-SIMS analysis.

Preparation of the Working Electrode for Electrocatalytic Water Splitting: First, the commercially purchased Ni foam (NF) was pretreated by washing with acetone, followed by 1 M HCl for 15 min each to remove any surface oxides. Then, these Ni foams were again rinsed with water and ethanol, dried in a vacuum oven, and used for electrode fabrication. The working electrode was prepared by mixing 10 mg of catalyst material (NiO nanosheet powder) and 2 mg of PVDF. This mixture was finely ground, and 100 µL of NMP was added to make the slurry and coated on the Ni foam over an area of 0.5 cm^2. To prepare the 20% Ni NC@NiO heterostructure electrode, 1 mL of Ni NC solution (2 mg mL^{-1}) was added to the 8 mg NiO and ground in a mortar and pestle along with PVDF for 45 min. These uniformly coated electrodes were dried overnight at 50 °C in a vacuum oven for further electrochemical measurements. The Ni NCs loading was controlled by adding different amounts of nanocluster solution into the NiO powder. The average loading for the working electrode was maintained at ≈2 mg cm^{-2}.

Electrochemical Measurements: A CHI708E electrochemical workstation was used to record all the electrochemical measurements in a 1 M KOH solution. The HER and OER performance were measured using a conventional three-electrode system with the catalyst-coated Ni foam as the working electrode, graphite rod as the counter electrode, and an Ag/AgCl (1 M KCl) as the reference electrode. This study's potential values were converted to a reversible hydrogen electrode (RHE) scale using the equation $E_{RHE} = E_{Ag/AgCl} + (0.22\,V + 0.059\,pH)$. The linear sweep voltammetry (LSV) measurements were recorded with a scan rate of 50 mV s^{-1}. To find the electrochemical active surface area (ESCA), CV were taken in the non-Faradic potential range of 0.746–1.106 V versus RHE with a 100–140 mV s^{-1} scan rate. Electrochemical AC impedance spectra were recorded in the frequency range from 10^5 to 0.1 Hz with 10 mV amplitude. The resulting impedance spectra were fitted using an analogous circuit model to find the solution and charge transfer resistance. A chronoamperometric measurement was used for 78000 s at a fixed potential to conduct the long-term durability tests. All the data were reported without any iR-correction.

Computational Methodology: All the calculations were performed using first-principles DFT as implemented in Vienna Ab Initio Simulation Package (VASP).[94–98] The projection operators were evaluated in real space utilizing Projector Augmented Wave[99] potentials and the Perdew–Burke–Ernzerhof[99] generalized gradient approximation as exchange-correlation functional. Structural optimization was performed without symmetry constraints, and the structures were considered converged upon reaching an interatomic force below 0.01 eV $Å^{-1}$ with a self-consistent energy convergence limit of 10^{-4} eV. Plane wave basis-set cutoff energy was considered to be 500 eV during the calculations. The reciprocal space integration across the 2D irreducible Brillouin zone was performed using the Monkhorst–Pack[100] of $3 \times 3 \times 1$ **k**-mesh. For molecule and cluster optimization, we used Γ-centered **k**-grid distribution. The Gaussian smearing method was used throughout the calculations with valence electronic configuration[98,101] of nickel ($3d^8\ 4s^2$), oxygen ($2s^2\ 2p^4$), sulfur ($3s^2\ 3p^4$), carbon ($2s^2\ 2p^2$), and hydrogen ($1s^1$). We considered the NiO (100) surface with a $(3 \times 3 \times 3)$ supercell; the number of atoms for adsorbed systems in the NiO-slab state and in the adsorbed state is 216 (108 Ni and 108 O atoms). 12 Å vacuum space was added along the transverse direction to mitigate the interactions between periodic replicas. We considered a $Ni_6S_{12}(CH_3)_6$ geometry for the nanocluster to model the interaction of S with the NiO surface. The structures were optimized in all three directions without any constraints.

Supporting Information

Supporting Information is available from the Wiley Online Library or from the author.

Acknowledgements

The authors acknowledge the financial support from the Science & Engineering Research Board (Project ID: SRG/2022/000135), IIT Kharagpur (Project code: DLR), and the Scheme for Promotion for Academic and Research Collaboration (Project ID: 3140). T.R.G. thanks the Ministry of Education, Govt. of India, for the PMR Fellowship. M.K.S. acknowledges the Anusandhan National Research Foundation (ANRF), India, for the financial support in the form of the National Post Doctoral Fellowship (N-PDF). The authors acknowledge the Central Research Facility (CRF) and Sophisticated Analytical and Technical Help Institute (SATHI) at IIT Kharagpur for sample measurements. The authors thank Shankha Shubhra Mondal, Shakil Ahammad Chowdhury, and Anindita Sarkar for their cooperation in a few experimental measurements and data analysis. T.R.G. and M.K.S. acknowledge all the group members of Indranath Research Group (IRG) for their valuable discussions and constant support throughout this work. P.S. and A.R. sincerely acknowledge the runtime in the Paramshakti Supercomputer at IIT Kharagpur, a flagship facility under the National Supercomputer Mission (NSM), Government of India. A.R. acknowledges funding from the BRNS, Department of Atomic Energy, Government of India.

Conflict of Interest

The authors declare no conflict of interest.

Author Contributions

Indranath Chakraborty: conceptualization (lead); funding acquisition (lead); project administration (lead); resources (lead); supervision (lead); writing—original draft (equal); writing—review and editing (lead). **Tapu Raihan Gazi**: data curation (lead); formal analysis (equal); investigation (equal); methodology (equal); writing—original draft (equal); writing—review and editing (equal). **Mrinal Kanti Sikdar**: data curation (lead); formal analysis (equal); investigation (lead); methodology (equal); writing—original draft (lead); writing—review and editing (equal) **Pijush Sardar**: data curation (supporting); formal analysis (equal); investigation (equal); methodology (equal); software (lead); writing—original draft (equal); writing—review and editing (supporting). **Ahin Roy**: formal analysis (equal); supervision (equal); writing—original draft (equal); writing—review and editing (supporting). **Tapu Raihan Gazi**, **Mrinal Kanti Sikdar**, and **Pijush Sardar** contributed equally to this work.

Data Availability Statement

The data that support the findings of this study are available in the supplementary material of this article.

Keywords

interface engineering, nanoheterostructures, Ni nanoclusters, structure–property, water splitting

Received: July 23, 2025
Revised: September 16, 2025
Published online:

[1] H. Ding, H. Liu, W. Chu, C. Wu, Y. Xie, *Chem. Rev.* **2021**, *121*, 13174.
[2] X. Li, X. Hao, A. Abudula, G. Guan, *J. Mater. Chem. A* **2016**, *4*, 11973.
[3] S. Marini, P. Salvi, P. Nelli, R. Pesenti, M. Villa, M. Berrettoni, G. Zangari, Y. Kiros, *Electrochim. Acta* **2012**, *82*, 384.

[4] K. Zeng, D. Zhang, *Prog. Energy Combust. Sci.* **2010**, *36*, 307.
[5] G. Chen, G. Chen, T. Wang, J. Zhang, P. Liu, H. Sun, X. Zhuang, M. Chen, X. Feng, *Adv. Mater.* **2018**, *30*, 1706279.
[6] Q. Xu, J. Zhang, H. Zhang, L. Zhang, L. Chen, Y. Hu, H. Jiang, C. Li, *Energy Environ. Sci.* **2021**, *14*, 5228.
[7] L. Jiang, L. Jiang, X. Luo, R. Li, Q. Zhou, L. Wang, L. Chen, S. Mu, *Chem. Eng. J.* **2024**, *502*, 157952.
[8] A. Kazemi, F. Manteghi, Z. Tehrani, *ACS Omega* **2024**, *9*, 7310.
[9] F. Guo, T. J. Macdonald, A. J. Sobrido, L. Liu, J. Feng, G. He, *Adv. Sci.* **2023**, *10*, 2301098.
[10] Y. Lin, Z. Tian, L. Zhang, J. Ma, Z. Jiang, B. J. Deibert, R. Ge, L. Chen, *Nat. Commun.* **2019**, *10*, 162.
[11] R. Qin, G. Chen, X. Feng, J. Weng, Y. Han, *Adv. Sci.* **2024**, *11*.
[12] R. Jin, C. Zeng, M. Zhou, Y. Chen, *Chem. Rev.* **2016**, *116*, 10346.
[13] I. Chakraborty, T. Pradeep, *Chem. Rev.* **2017**, *117*, 8208.
[14] Y. Negishi, K. Nobusada, T. Tsukuda, *J. Am. Chem. Soc.* **2005**, *127*, 5261.
[15] K. Sahoo, T. R. Gazi, S. Roy, I. Chakraborty, *Commun. Chem.* **2023**, *6*, 157.
[16] R. Jin, *Nanoscale* **2015**, *7*, 1549.
[17] A. Heuer-Jungemann, N. Feliu, I. Bakaimi, M. Hamaly, A. Alkilany, I. Chakraborty, A. Masood, M. F. Casula, A. Kostopoulou, E. Oh, K. Susumu, M. H. Stewart, I. L. Medintz, E. Stratakis, W. J. Parak, A. G. Kanaras, *Chem. Rev.* **2019**, *119*, 4819.
[18] Y. Zeng, S. Havenridge, M. Gharib, A. Baksi, K. L. D. M. Weerawardene, A. R. Ziefuß, C. Strelow, C. Rehbock, A. Mews, S. Barcikowski, M. M. Kappes, W. J. Parak, C. M. Aikens, I. Chakraborty, *J. Am. Chem. Soc.* **2021**, *143*, 9405.
[19] S. Zhao, R. Jin, Y. Song, H. Zhang, S. D. House, J. C. Yang, R. Jin, *Small* **2017**, *13*.
[20] M. Ghosal Chowdhury, L. Sahoo, S. Maity, D. Bain, U. K. Gautam, A. Patra, *ACS Appl. Nano Mater.* **2022**, *5*, 7132.
[21] V. Saini, S. Choudhary, A. Gaur, S. Banerjee, V. Bagchi, V. Venkatesh, *J. Mater. Chem. A* **2023**, *11*, 24754.
[22] J. Wei, R. Zhao, D. Luo, X. Lu, W. Dong, Y. Huang, X. Cheng, Y. Ni, *J. Colloid Interface Sci.* **2023**, *631*, 212.
[23] L. Sahoo, A. Devi, A. Patra, *ACS Sustainable Chem. Eng.* **2023**, *11*, 4187.
[24] Z. Yin, Z. Wang, X. Dai, N. Liu, S. Wang, G. Li, F. Du, X. Yuan, *ACS Sustainable Chem. Eng.* **2020**, *8*, 15336.
[25] Q.-L. Mo, B.-J. Liu, F.-X. Xiao, *J. Phys. Chem. C* **2021**, *125*, 22421.
[26] M. A. Abbas, R. Khan, S. J. Yoon, J. H. Bang, *ACS Appl. Mater. Interfaces* **2020**, *12*, 16566.
[27] H. Xu, D. Rebollar, H. He, L. Chong, Y. Liu, C. Liu, C.-J. Sun, T. Li, J. V. Muntean, R. E. Winans, D.-J. Liu, T. Xu, *Nat. Energy* **2020**, *5*, 623.
[28] L. Chen, L. Klemeyer, M. Ruan, X. Liu, S. Werner, W. Xu, A. Koeppen, R. Bücker, M. G. Gonzalez, D. Koziej, W. J. Parak, I. Chakraborty, *Small* **2023**, *19*, 2206772.
[29] M. Gharib, A. Kornowski, H. Noei, W. J. Parak, I. Chakraborty, *ACS Mater. Lett.* **2019**, *1*, 310.
[30] X. Yuan, Y. Tay, X. Dou, Z. Luo, D. T. Leong, J. Xie, *Anal. Chem.* **2013**, *85*, 1913.
[31] L. Zhu, Y. Zeng, M. Teubner, B. Grimm-Lebsanft, A. R. Ziefuß, C. Rehbock, M. A. Rübhausen, S. Barcikowski, W. J. Parak, I. Chakraborty, *ACS Appl. Nano Mater.* **2021**, *4*, 3197.
[32] Z.-W. Ma, Z. Ren, X.-Y. Dong, F. Pan, *Inorg. Chem.* **2025**, *64*, 11370.
[33] Nonappa, *Chem. Commun.* **2023**, *59*, 13800.
[34] Z. Wu, Y. Li, J. Liu, Z. Lu, H. Zhang, B. Yang, *Angew. Chem.* **2014**, *126*, 12392.
[35] A. Chakraborty, G. Fu, Y. Tian, X. Li, M. Luo, X. Wei, T. Zhang, T. Gao, C. Chen, S. Chaemchuen, X. Xu, X. Sun, T. Bu, F. Verpoort, J. Wang, Z. Kou, *Angew. Chem. Int. Ed.* **2018**, *57*, 6522.
[36] D. Wang, Q. Li, C. Han, Z. Xing, X. Yang, *ACS Cent. Sci.* **2018**, *4*, 112.
[37] J. Chen, G. Fu, Y. Tian, X. Li, M. Luo, X. Wei, T. Zhang, T. Gao, C. Chen, S. Chaemchuen, X. Xu, X. Sun, T. Bu, F. Verpoort, J. Wang, Z. Kou, *Interdiscip. Mater.* **2024**, *3*, 595.
[38] P. Ji, D. Zheng, H. Jin, D. Chen, X. Luo, J. Yang, Z. Wang, S. Mu, *Small Struct.* **2023**, *4*, 2300013.
[39] K. Lu, Y. Liu, F. Lin, I. A. Cordova, S. Gao, B. Li, B. Peng, H. Xu, J. Kaelin, D. Coliz, C. Wang, Y. Shao, Y. Cheng, et al., *J. Am. Chem. Soc.* **2020**, *142*, 12613.
[40] A. Song, S. Song, M. Duanmu, H. Tian, H. Liu, X. Qin, G. Shao, G. Wang, *Small Sci.* **2023**, *3*, 2300036.
[41] F. Song, L. Bai, A. Moysiadou, S. Lee, C. Hu, L. Liardet, X. Hu, *J. Am. Chem. Soc.* **2018**, *140*, 7748.
[42] Y. Mu, R. Ma, S. Xue, H. Shang, W. Lu, L. Jiao, *Carbon Neutralization* **2024**, *3*, 4.
[43] D. Papurello, A. Lanzini, S. Fiorilli, F. Smeacetto, R. Singh, M. Santarelli, *Chem. Eng. J.* **2016**, *283*, 1224.
[44] Y. Wen, K. Zhao, J. Lu, K. Huang, *Energy Fuels* **2025**, *39*, 8291.
[45] X. Cui, H. He, D. Xie, L. Zheng, X. Wang, Z. Jiang, D. Xu, Y. Guo, *Chem. Eng. J.* **2023**, *464*, 142622.
[46] B. Long, H. Yang, M. Li, M.-S. Balogun, W. Mai, G. Ouyang, Y. Tong, P. Tsiakaras, S. Song, *Appl. Catal. B Environ.* **2019**, *243*, 365.
[47] J. Zhang, F. Wang, C.-S. Lian, *Phys. Rev. B* **2024**, *110*, 245416.
[48] X. Yan, Y. Jiang, Q. Jin, T. Yao, W. Wang, A. Tao, C. Gao, X. Li, C. Chen, H. Ye, X.-L. Ma, *Nat. Commun.* **2023**, *14*, 2788.
[49] K. Wang, R. Chen, H. Yang, Y. Chen, H. Jia, Y. He, S. Song, Y. Wang, *Adv. Funct. Mater.* **2024**, *34*, 2310683.
[50] F. Ando, T. Gunji, T. Tanabe, I. Fukano, H. D. Abruña, J. Wu, T. Ohsaka, F. Matsumoto, *ACS Catal.* **2021**, *11*, 9317.
[51] S. J. Tauster, S. C. Fung, R. L. Garten, *J. Am. Chem. Soc.* **1978**, *100*, 170.
[52] K. Wang, H. Yang, Q. Wang, J. Yu, Y. He, Y. Wang, S. Song, Y. Wang, *Adv. Energy Mater.* **2023**, *13*, 2204371.
[53] W. Zhang, J. Chang, Y. Yang, *SusMat* **2023**, *3*, 2.
[54] F. Wang, L. Hu, R. Liu, H. Yang, T. Xiong, Y. Mao, M.-S. Jie, T. Balogun, G. Ouyang, Y. Tong, *J. Mater. Chem. A* **2019**, *7*, 11150.
[55] R. Zhang, M. Zhang, H. Yang, G. Li, S. Xing, M. Li, Y. Xu, Q. Zhang, S. Hu, H. Liao, Y. Cao, *Small Methods* **2021**, *5*, 2100612.
[56] Z. Mo, K. Wang, H. Yang, Z. Ou, Y. Tong, T. Yu, Y. Wang, P. Tsiakaras, S. Song, *Appl. Catal. B Environ.* **2020**, *277*, 119249.
[57] J. Wang, S. Mao, Z. Liu, Z. Wei, H. Wang, Y. Chen, Y. Wang, *ACS Appl. Mater. Interfaces* **2017**, *9*, 7139.
[58] Y. Sun, *Appl. Surf. Sci.* **2023**, *637*, 157870.
[59] J. Zhang, X. Li, X. Zhang, C. Cheng, L. Xiao, M. Zhou, C. Dong, H. Liu, X. Du, J. Yang, *Small Methods* **2023**, *7*, 2300461.
[60] Z. Zhuang, W. Chen, *Analyst* **2020**, *145*, 2621.
[61] O. V. Dolomanov, L. J. Bourhis, R. J. Gildea, J. A. K. Howard, H. Puschmann, *J. Appl. Crystallogr.* **2009**, *42*, 339.
[62] S. A. Claridge, A. W. Castleman, S. N. Khanna, C. B. Murray, A. Sen, P. S. Weiss, *ACS Nano* **2009**, *3*, 244.
[63] A. Nag, T. Pradeep, *ACS Nanosci. Au* **2022**, *2*, 160.
[64] S. Das, T. Sekine, H. Mabuchi, S. Hossain, S. Das, S. Aoki, S. Takahashi, Y. Negishi, *Chem. Commun.* **2023**, *59*, 4000.
[65] P. Chandrashekar, D. A. Varghese, T. Thomas, A. K. Pal, A. Muraleedharan, A. Salam, M. Ghosh, P. K. Mondal, S. V. Suresh, C. K. Nandi, A. Datta, S. Mandal, *J. Phys. Chem. Lett.* **2025**, *16*, 4107.
[66] R. R. Manikkoth, P. Baidya, S. S. Rajasree, P. Chandrashekar, M. P. Maman, P. Deria, S. Mandal, *Cryst. Growth Des.* **2024**, *24*, 4213.
[67] A. K. Das, S. Biswas, A. Kayal, A. C. Reber, S. Bhandary, D. Chopra, J. Mitra, S. N. Khanna, S. Mandal, *Nano Lett.* **2023**, *23*, 8923.
[68] A. K. Mondal, D. Su, Y. Wang, S. Chen, G. Wang, *Chem. – Asian J.* **2013**, *8*, 2828.

[69] M. Huang, F. Li, J. Y. Ji, Y. X. Zhang, X. L. Zhao, X. Gao, *CrystEngComm* **2014**, *16*, 2878.
[70] Y. Su, G. Yuan, J. Hu, G. Zhang, Y. Tang, Y. Chen, Y. Tian, S. Wang, M. Shakouri, H. Pang, *Adv. Mater.* **2024**, *36*, 2406094.
[71] Q. He, Y. Wan, H. Jiang, Z. Pan, C. Wu, M. Wang, X. Wu, B. Ye, P. M. Ajayan, L. Song, *ACS Energy Lett.* **2018**, *3*, 1373.
[72] Y. Wang, M. Qiao, Y. Li, S. Wang, *Small* **2018**, *14*, 1800136.
[73] V. Jeseentharani, N. Pugazhenthiran, A. Mathew, I. Chakraborty, A. Baksi, J. Ghosh, M. Jash, G. S. Anjusree, T. G. Deepak, A. S. Nair, T. Pradeep, *ChemistrySelect* **2017**, *2*, 1454.
[74] S. Nagappan, R. Jayan, N. Rajagopal, A. V. Krishnan, M. M. Islam, S. Kundu, *Small* **2024**, *20*.
[75] H. Li, H. Pang, W. Ma, E. Picheau, W. Jevasuwan, N. Fukata, Y. Sugahara, T. Sasaki, R. Ma, *Chem. Eng. J.* **2025**, *516*, 163916.
[76] Z. Wu, R. Liu, J. Wang, J. Zhu, W. Xiao, C. Xuan, W. Lei, D. Wang, *Nanoscale* **2016**, *8*, 19086.
[77] D. C. Frost, W. R. Leeder, R. L. Tapping, B. Wallbank, *Fuel* **1977**, *56*, 277.
[78] A. Munir, T. U. Haq, A. Qurashi, H. U. Rehman, A. Ul-Hamid, I. Hussain, *ACS Appl. Energy Mater.* **2019**, *2*, 363.
[79] O. Van Der Heijden, S. Park, R. E. Vos, J. J. J. Eggebeen, M. T. M. Koper, *ACS Energy Lett.* **2024**, *9*, 1871.
[80] A. Sadhukhan, A. Karmakar, K. Koner, S. Karak, R. K. Sharma, A. Roy, P. Sen, K. K. Dey, V. Mahalingam, B. Pathak, S. Kundu, R. Banerjee, *Adv. Mater.* **2024**, *36*, 2310938.
[81] B. Wang, F. Zhang, *Angew. Chem. Int. Ed.* **2022**, *61*, e202111026.
[82] J. Tian, M. Wang, J. Xie, J. Hu, Z. Lu, Y. Cao, *Fuel* **2025**, *394*, 135019.
[83] B. Jin, J. Sainio, J. Shi, H. Jiang, B. Ali, N. Han, T. Kallio, *Chem. Eng. J.* **2025**, *520*, 165999.
[84] S. Anantharaj, H. Sugime, S. Noda, *Chem. Eng. J.* **2021**, *408*, 127275.
[85] V. Saravanakumar, M. Mahendran, A. Vijayaprabhakaran, R. Madhu, M. Kathiresan, A. Sambandam, V. Suryanarayanan, S. Kundu, *ACS Appl. Energy Mater.* **2024**, *7*, 10650.
[86] N. K. Shrestha, S. A. Patil, J. Han, S. Cho, A. I. Inamdar, H. Kim, H. Im, *J. Mater. Chem. A* **2022**, *10*, 8989.
[87] J. Xiang, B. Xiang, X. Cui, *New J. Chem.* **2018**, *42*, 10791.
[88] X. Ding, D. Liu, P. Zhao, X. Chen, H. Wang, F. E. Oropeza, G. Gorni, M. Barawi, M. García-Tecedor, V. A. De La Peña O'Shea, J. P. Hofmann, J. Li, J. Kim, S. Cho, R. Wu, K. H. L. Zhang, *Nat. Commun.* **2024**, *15*.
[89] H. Chen, R. Ding, B. Liu, F. Zeng, H. Zhao, *Small* **2024**, *20*, 2306274.
[90] J. K. Nørskov, F. Abild-Pedersen, F. Studt, T. Bligaard, *Proc. Natl. Acad. Sci.* **2011**, *108*, 937.
[91] J. Li, R. R. Nasaruddin, Y. Feng, J. Yang, N. Yan, J. Xie, *Chem. – Eur. J.* **2016**, *22*, 14816.
[92] J. Qian, Z. Yang, J. Lyu, Q. Yao, J. Xie, *Precis. Chem.* **2024**, *2*, 495.
[93] P. Gahtori, V. Gunwant, R. Pandey, *Langmuir* **2024**, *40*, 21211.
[94] G. Kresse, J. Furthmüller, *Comput. Mater. Sci.* **1996**, *6*, 15.
[95] G. Kresse, J. Furthmüller, *Phys. Rev. B* **1996**, *54*, 11169.
[96] G. Kresse, J. Hafner, *Phys. Rev. B* **1993**, *47*, 558.
[97] P. E. Blöchl, *Phys. Rev. B* **1994**, *50*, 17953.
[98] G. Kresse, J. Hafner, *J. Phys. Condens. Matter* **1994**, *6*, 8245.
[99] J. P. Perdew, K. Burke, M. Ernzerhof, *Phys. Rev. Lett.* **1996**, *77*, 3865.
[100] H. J. Monkhorst, J. D. Pack, *Phys. Rev. B* **1976**, *13*, 5188.
[101] R. D. King-Smith, M. C. Payne, J. S. Lin, *Phys. Rev. B* **1991**, *44*, 13063.